Interlayer transport through a graphene/rotated boron nitride/graphene heterostructure

Supeng Ge,[1,*] K. M. Masum Habib,[2,†] Amrit De,[2] Yafis Barlas,[1,2] Darshana Wickramaratne,[2,‡] Mahesh R. Neupane,[2,§] and Roger K. Lake[2,‖]

[1]*Department of Physics and Astronomy, University of California, Riverside, California 92521-0204, USA*

[2]*Department of Electrical and Computer Engineering, University of California, Riverside, California 92521-0204, USA*

(Received 5 September 2016; revised manuscript received 19 November 2016; published 6 January 2017)

Interlayer electron transport through a graphene/hexagonal boron-nitride (h-BN)/graphene heterostructure is strongly affected by the misorientation angle θ of the h-BN with respect to the graphene layers with different physical mechanisms governing the transport in different regimes of angle, Fermi level, and bias. The different mechanisms and their resulting signatures in resistance and current are analyzed using two different models, a tight-binding, nonequilibrium Green function model and an effective continuum model, and the qualitative features resulting from the two different models compare well. In the large-angle regime ($\theta > 4^\circ$), the change in the effective h-BN band gap seen by an electron at the K point of the graphene causes the resistance to monotonically increase with angle by several orders of magnitude, reaching a maximum at $\theta = 30^\circ$. It does not affect the peak-to-valley current ratios in devices that exhibit negative differential resistance. In the small-angle regime ($\theta < 4^\circ$), umklapp processes open up new conductance channels that manifest themselves as nonmonotonic features in a plot of resistance versus Fermi level that can serve as experimental signatures of this effect. For small angles and high bias, the umklapp processes give rise to two new current peaks on either side of the direct tunneling peak.

DOI: 10.1103/PhysRevB.95.045303

I. INTRODUCTION

Graphene (Gr), a two-dimensional (2D) material made of carbon atoms arranged in a honeycomb structure, has excellent electronic, thermal, and mechanical properties that make it a promising candidate for nanoelectronic devices [1,2]. 2D hexagonal boron nitride (h-BN) has the same 2D honeycomb structure as graphene. Its lattice constant is closely matched to that of graphene, and its large band gap and good thermal and chemical stability make it an excellent insulator, substrate, and encapsulating material for graphene and other 2D materials [3,4]. There have been a number of experimental and theoretical studies of the in-plane electronic properties of graphene on h-BN [5–10]. In general, in a h-BN graphene heterolayer system, whether grown by chemical vapor deposition or assembled by mechanical stacking, the graphene will not be crystallographically aligned with the h-BN. The misalignment results in a small change in the in-plane graphene electron velocity [8].

Interest in the effect of misorientation on cross-plane transport began with bilayer graphene, and the first coherent tunneling calculations showed a 16 order of magnitude change in the interlayer resistance as a function of the misalignment angle [11]. Including phonon-mediated transport reduced the dependence on angle to a few orders of magnitude [12]. Replacing the source and drain misoriented graphene sheets with source and drain misoriented graphite leads resulted in the same angular dependence and very similar quantitative values for the coherent current [13]. This demonstrated sensitivity to interlayer misorientation motivates us to examine the effect in Gr/h-BN/Gr devices.

There is also significant interest in Gr/h-BN/Gr heterostructures for electronic device applications [14–33]. Gr/h-BN/Gr structures display negative differential resistance (NDR) [20,24,27,30–32,34], and theoretical calculations predict maximum frequencies of several hundred GHz [26]. The NDR arises from the lineup of the source and drain graphene Dirac cones combined with the conservation of in-plane momentum. In one experiment in which plateaus were observed in the current-voltage characteristics instead of NDR, the experimental results could be matched theoretically by ignoring momentum conservation [23]. In the theoretical treatments, the focus has been primarily on the rotation between top and bottom graphene layers and the resulting misalignment of the Dirac cones [20,27,32]. Recently, the effect of misalignment of both the h-BN and the graphene layers including the effects of phonon scattering have been investigated using the low-angle effective continuum model [30,35].

In this work, we focus on the effect of the h-BN misalignment and consider a system of two aligned graphene layers serving as the source and the drain separated by one or more AB stacked layers of h-BN that are misoriented with respect to the graphene. An illustration of such a system is shown in Fig. 1(a). This system is analyzed using two different models and the results from the two models are compared. Commensurate rotation angles in the range $1.89^\circ \leqslant \theta \leqslant 27.8^\circ$ are simulated with a tight-binding model and the nonequilibrium Green's function (NEGF) formalism. The small-angle regime is also analyzed with a continuum model similar to that used in Ref. [35]. The qualitative features of the two different models compare well, and the continuum model elucidates the physics of the small-angle regime

The misorientation of the h-BN with respect to the graphene can have several possible effects that dominate in different regimes of angle and applied bias. (a) For devices under high bias, it can alter the transverse momentum conservation and

*supeng.ge@email.ucr.edu

†Present address: Intel Corp., Santa Clara CA 95054, USA.

‡Present address: Materials Department, University of California, Santa Barbara, CA 93106-5050.

§Present address: U. S. Army Research Laboratory, RDRL-WMM-G, Aberdeen Proving Ground, Maryland 21005, USA.

‖rlake@ece.ucr.edu

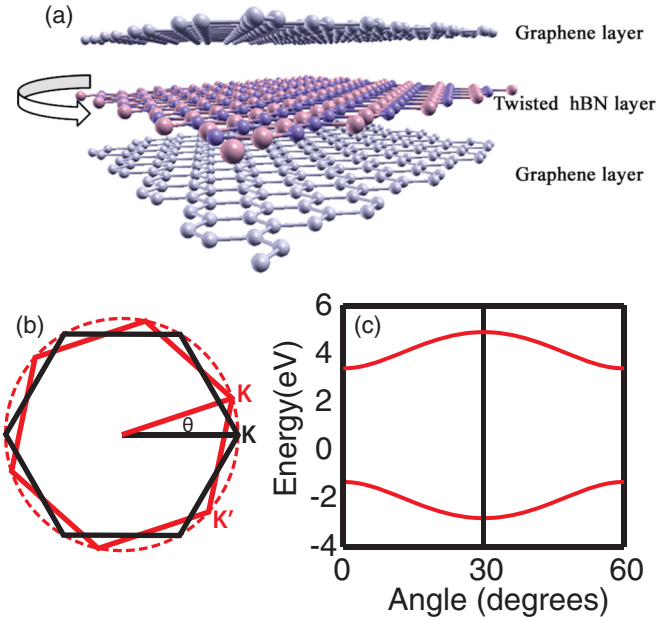

FIG. 1. (a) Atomistic geometry of the graphene/boron nitride/graphene heterostructure. The top and bottom layers are aligned graphene. The middle boron nitride layer is rotated with respect to the graphene layers. (b) In k space, the relative rotation between the Brillouin zone of h-BN (red) with respect to that of graphene (black). (c) The energy gap of monolayer h-BN at the K point of graphene as a function of rotation angle.

thus degrade the NDR. (b) It can alter the potential barrier seen by the electrons at the K points in the graphene, and thus alter the interlayer tunneling current and resistance. (c) As in misoriented graphene on graphene, it can result in destructive quantum interference that reduces the current. A signature of this effect is that over a range of angles, the coherent interlayer resistance scales monotonically with the size of the commensurate unit cell [12,13]. (d) For small-angle rotations, umklapp processes can open up new channels of conductance resulting in new features that depend on Fermi level, angle, and bias. The presence or absence of these effects and under what conditions they manifest themselves will become clear in the analysis.

The paper is organized as follows. Section II A describes the tight-binding model and the NEGF method used to calculate the coherent resistance for different commensurate angles and different h-BN layer thicknesses. Section II B describes the effective continuum model employed to analyze the low-angle regime. Section III describes and discusses the results. Conclusions are given in Sec. IV. The Appendixes gives details of the tight-binding model and calculations.

II. MODELS AND METHODS

A. Tight-binding transport calculations

The interlayer transport in the Gr/h-BN/Gr device illustrated in Fig. 1 is analyzed using a tight-binding Hamiltonian and a nonequilibrium Green's function (NEGF) approach for the transport. The device Hamiltonian has the following

TABLE I. Parameters for the tight-binding model. t_0 is the intralayer, off-diagonal matrix element. All other parameters are described by Eq. (2).

	In-plane interaction	Interlayer interaction				
	t_0(eV)	$t_\perp$(eV)	$d_\perp$(Å)	λ_z(Å)	λ_{xy}(Å)	α
C-*C*	2.85	0.39	3.35	0.60	1.70	1.65
B-*N*	2.52	0.60				
C-*B*		0.62	3.22	0.54	0.84	2.04
C-*N*		0.38	3.22	0.41	0.97	2.03

block-tridiagonal form:

$$\mathbf{H} = \begin{pmatrix} \mathbf{H}_T(\mathbf{k}) & \mathbf{t}_T(\mathbf{k}) & 0 \\ \mathbf{t}_T^\dagger(\mathbf{k}) & \mathbf{H}_{\mathrm{BN}}(\mathbf{k}) & \mathbf{t}_B(\mathbf{k}) \\ 0 & \mathbf{t}_B^\dagger(\mathbf{k}) & \mathbf{H}_B(\mathbf{k}) \end{pmatrix}, \tag{1}$$

where $\mathbf{k}$ is the wave vector in the x-y plane, $\mathbf{H}_{T(B)}$ is the Hamiltonian of the uncoupled top (bottom) graphene layers, $\mathbf{H}_{\mathrm{BN}}$ is the Hamiltonian of the h-BN layer(s), and $\mathbf{t}_{T(B)}$ is the block of matrix elements coupling $\mathbf{H}_{T(B)}$ to $\mathbf{H}_{\mathrm{BN}}$. The elements t_{ij} of the off-diagonal blocks $\mathbf{t}_{T(B)}$ representing the interaction between atom i in a graphene layer and atom j in the adjacent h-BN layer are given by [12]

$$t_{ij} = t_\perp \exp\left(-\frac{r_{ij} - d_\perp}{\lambda_z}\right) \exp\left[\left(\frac{\xi_{ij}}{\lambda_{xy}}\right)^\alpha\right], \tag{2}$$

where $d_\perp$ is the interlayer disatnce, r_{ij} is the distance between two atoms i and j, and $\xi_{ij} = [(x_i - x_j)^2 + (y_i - y_j)^2]^{1/2}$ is the projected in-plane distance between the two atoms. The lattice constant of the entire system is set to that of graphene. The misoriented commensurate primitive unit cells are created using the approach described in Ref. [36]. Parameters for this tight-binding model were extracted by fitting the band structures to density functional theory (DFT) results. The onsite energy for C is set to 0 and the onsite energies of the B and N atoms are 3.40 and -1.31 eV, respectively. For multiple h-BN layers, we adapt the interlayer h-BN interaction strength $t' = 0.60$ eV from Ref. [37]. All other parameters are shown in Table I.

Since this is essentially a 2D-2D tunneling problem, the coherent interlayer transmission through the Gr/h-BN/Gr structure is calculated within a NEGF approach using the "generalized boundary conditions" described in Ref. [38]. Within the NEGF approach, the graphene layers act as the "contacts" and the h-BN layer acts as the "device." The surface Green's functions of the top and bottom graphene layers are

$$\mathbf{g}_{T(B)}(E,\mathbf{k}) = \left[\left(E + i\frac{\gamma}{2}\right)\mathbf{I} - \mathbf{H}_{T(B)}(\mathbf{k})\right]^{-1}, \tag{3}$$

where $\mathbf{I}$ is the identity matrix, and the energy broadening $\gamma = 80$ meV is chosen to match that of Ref. [11]. Given the surface Green's functions, the rest of the NEGF calculations follow as usual. Here, the "device" Green's function is

$$\mathbf{G}^r(E,\mathbf{k}) = [E\mathbf{I} - \mathbf{H}_{\mathrm{BN}}(\mathbf{k}) - \mathbf{\Sigma}_T(E,\mathbf{k}) - \mathbf{\Sigma}_B(E,\mathbf{k})]^{-1}, \tag{4}$$

where the self-energies resulting from coupling to the graphene layers are $\mathbf{\Sigma}_T = \mathbf{t}_T^\dagger \mathbf{g}_T \mathbf{t}_T$ and $\mathbf{\Sigma}_B = \mathbf{t}_B \mathbf{g}_B \mathbf{t}_B^\dagger$. The transmission

coefficient is

$$T(E,\mathbf{k}) = \mathrm{tr}[\mathbf{\Gamma}_T \mathbf{G}^r \mathbf{\Gamma}_B \mathbf{G}^{r\dagger}], \tag{5}$$

where $\mathbf{\Gamma}_T = \mathbf{t}_T^\dagger \mathbf{a}_T \mathbf{t}_T$, $\mathbf{\Gamma}_B = \mathbf{t}_B \mathbf{a}_B \mathbf{t}_B^\dagger$, $\mathbf{a}_{T(B)} = -i(\mathbf{g}_{T(B)} - \mathbf{g}_{T(B)}^\dagger)$ is the spectral function of the top (bottom) graphene layer, and tr[. . .] indicates a trace of the matrix.

Integrating Eq. (5) for the transmission over the first commensurate Brillouin zone, the energy-dependent transmission coefficient per unit area is

$$T(E) = \int_{1\mathrm{st\ BZ_c}} \frac{d^2\mathbf{k}}{4\pi^2} T(E,\mathbf{k}). \tag{6}$$

This integration is performed numerically on a square grid with $\Delta k_x = \Delta k_y = 0.005$ Å^{-1} (see Appendix A for further details). The linear conductance is given by

$$G = 2\frac{e^2}{h} \int dE T(E) \left(-\frac{\partial f}{\partial E}\right), \tag{7}$$

where the factor of 2 accounts for the spin degeneracy, and the integration over $\mathbf{k}$ accounts for the valley degeneracy. The resistance is the inverse of the conductance, $R = 1/G$.

For finite-bias calculations, an applied bias $V_b = \Delta/e$ is symmetrically applied across the device by setting $\mathbf{H}_T^{i,j} = \delta_{ij}\Delta/2$ and $\mathbf{H}_B^{i,j} = -\delta_{ij}\Delta/2$. When multiple h-BN layers are present, the potential drops linearly within the h-BN region since h-BN is an insulator. The tunneling current flowing through the device is given by

$$I = \frac{2e}{h} \int dE T(E)[f(E-\mu_T) - f(E-\mu_B)], \tag{8}$$

where $\mu_T = \mu_t + \Delta/2$ and $\mu_B = \mu_b - \Delta/2$ are the chemical potentials of the top and bottom graphene, respectively, $f(E)$ is the Fermi distribution function, and $\Delta V = \mu_t - \mu_b$ is the potential difference between the charge neutral points of the two Gr layers. ΔV accounts for the effect of gating and doping. We refer to ΔV as the built-in potential in analogy with a pn junction since this is the potential that exists before the bias is applied.

B. Effective continuum model

As the rotation angles become smaller, the commensurate unit cells become very large. As a result, NEGF calculations with the large tight-binding Hamiltonians become computationally challenging. In order to better understand the physics governing the interlayer transport at small rotation angles, we construct an effective continuum model. In the small-angle region ($\theta < 10^\circ$), the coupling matrix between graphene and h-BN layer is of the following form [20,30,39]:

$$\mathbf{H}_{int} = \frac{1}{3} \sum_{j=1,2,3} e^{-i\mathbf{q}_j(\theta)\cdot\mathbf{r}} \mathbf{T}_j, \tag{9}$$

where

$$\mathbf{T}_j = \begin{pmatrix} t_{CB}\eta^{(j-1)} & t_{CN}\eta^{-(j-1)} \\ t_{CB} & t_{CN}\eta^{(j-1)} \end{pmatrix}. \tag{10}$$

In Eq. (10), the row indices correspond to the A and B atoms of the graphene, and the column indices correspond to the B and N atoms of the h-BN. The lower off-diagonal element corresponds to a C atom directly over a B atom. All other elements correspond to a C atom in the center of an equilateral triangle of B atoms or N atoms. The hopping amplitudes t_{CB} and t_{CN} between a C atom and a B or N atom are the same as those listed in Table I. The phase factors $\eta = e^{i(2\pi/3)}$ result from the matrix elements of the Bloch sums evaluated at the K points. The index j labels the three equivalent corners of graphene's Brillouin zone corresponding to the three $\mathbf{K}$ points. The momentum shift $\mathbf{q}_j(\theta)$ is the momentum misalignment between the three equivalent $\mathbf{K}$ points of the h-BN and those of the graphene. Specifically,

$$\begin{aligned} \mathbf{q}_1(\theta) &= k_D(0,\theta), \\ \mathbf{q}_2(\theta) &= k_D\left(-\frac{\sqrt{3}}{2}\theta, -\frac{1}{2}\theta\right), \\ \mathbf{q}_3(\theta) &= k_D\left(\frac{\sqrt{3}}{2}\theta, -\frac{1}{2}\theta\right), \end{aligned} \tag{11}$$

where $k_D = \frac{4\pi}{3a}$ is the magnitude of the K point of graphene. When $\theta = 0$, $\mathbf{q} = 0$, and the sum in Eq. (9) will cause the diagonal and upper off-diagonal elements of $\mathbf{H}_{int}$ to vanish, leaving a coupling matrix corresponding to AB stacking with the B atom directly above the C atom.

By eliminating H_{BN} from Hamiltonian (1), we reduce the 3×3 Hamiltonian into an effective 2×2 Hamiltonian and obtain the effective interaction Hamiltonian between the top and bottom graphene layers as [40]

$$\mathbf{U}_{TB}(\epsilon) = \mathbf{H}_{int}(\epsilon - \mathbf{H}_{\mathrm{BN}})^{-1}\mathbf{H}_{int}^\dagger. \tag{12}$$

The low-energy electronic structure of h-BN can be described by a gapped Dirac-type Hamiltonian that acts on the B and N p_z orbital basis around a given K point,

$$\mathbf{H}_{\mathrm{BN}}(\Delta\mathbf{K}) = \begin{pmatrix} \epsilon_B & \hbar\upsilon_{BN}\Delta K e^{i\theta_{\Delta K}} \\ \hbar\upsilon_{BN}\Delta K e^{-i\theta_{\Delta K}} & \epsilon_N \end{pmatrix}. \tag{13}$$

The energies ϵ_B and ϵ_N are the onsite energies of the B and N atoms, while υ_{BN} is the velocity that is determined by the in-plane matrix elements between the B and N atoms given in Table I. The $\Delta\mathbf{K}$ is the connection vector between $\mathbf{K}$ point of graphene and h-BN. Then, we obtain

$$\begin{aligned} (\epsilon - \mathbf{H}_{\mathrm{BN}})^{-1} = &\frac{1}{(\epsilon-\epsilon_N)(\epsilon-\epsilon_B) - (\hbar\upsilon_{BN}\Delta K)^2} \\ &\times \begin{pmatrix} \epsilon-\epsilon_N & 0 \\ 0 & \epsilon-\epsilon_B \end{pmatrix}. \end{aligned} \tag{14}$$

The off-diagonal term vanished due to the threefold symmetry of $\Delta\mathbf{K}$. Combining Eqs. (9), (12), and (14), the effective interaction Hamiltonian is

$$\mathbf{U}_{TB}(\epsilon) = \frac{1}{9} \sum_{i,j=1,2,3} e^{i\mathbf{G}_{ij}(\theta_T,\theta_B)\mathbf{r}} \mathbf{T}_i (\epsilon - \mathbf{H}_{\mathrm{BN}})^{-1} \mathbf{T}_j, \tag{15}$$

where $\mathbf{G}_{ij}(\theta_T,\theta_B) = \mathbf{q}_i(\theta_T) - \mathbf{q}_j(\theta_B)$ is the momentum difference shift during transmission. Since the top and bottom graphene layers are aligned ($\theta_T = \theta_B$),

$$|G_{ij}| = \begin{cases} 0 & \text{for } i = j, \\ \sqrt{3}k_D\theta_T & \text{for } i \neq j. \end{cases} \tag{16}$$

This can be interpreted as the momentum being conserved for transmission between aligned Dirac cones of the top and bottom graphene layers. For transmission between misaligned Dirac cones, the momentum shifts by $|G_{ij}| = \sqrt{3}k_D\theta_T$.

The tunneling matrix element for the transmission between the top and bottom layers is

$$T_{\alpha,\beta}(\mathbf{k}_T,\mathbf{k}_B) = \sum_{i,j=1,2,3} t_{i,j}^{\alpha,\beta}(\mathbf{k}_T,\mathbf{k}_B)\delta(\mathbf{k}_T - \mathbf{k}_B - \mathbf{G}_{ij}), \quad (17)$$

where

$$t_{i,j}^{\alpha,\beta}(\mathbf{k}_T,\mathbf{k}_B) = \tfrac{1}{9}\phi_\alpha^\dagger(\mathbf{k}_T)\mathbf{T}_i(\epsilon - \mathbf{H}_{\rm BN})^{-1}\mathbf{T}_j\phi_\beta(\mathbf{k}_B) \quad (18)$$

and the eigenvectors of the graphene layers are $\phi_\alpha(\mathbf{k}) = \frac{1}{\sqrt{2}}[1,\alpha e^{i\theta_\mathbf{k}}]e^{i\mathbf{k}\cdot\mathbf{r}}$, where $\alpha = \pm 1$ is the band index. The linear conductance is [11]

$$G = \frac{e^2 g_s g_v}{\hbar\mathcal{A}} \sum_{\substack{\mathbf{k}_T,\mathbf{k}_B \\ \alpha,\beta}} |T_{\alpha,\beta}(\mathbf{k}_T,\mathbf{k}_B)|^2 \times A[\epsilon_\alpha(\mathbf{k}_T),\epsilon_F]A[\epsilon_\beta(\mathbf{k}_B),\epsilon_F] \quad (19)$$

or

$$G = \frac{e^2 g_s g_v}{\hbar\mathcal{A}} \sum_{\substack{\mathbf{k},\alpha,\beta \\ i,j\,=\,1,2,3}} \left|t_{i,j}^{\alpha,\beta}(\mathbf{k},\mathbf{k}+\mathbf{G}_{ij})\right|^2 \times A[\epsilon_\alpha(\mathbf{k}),\epsilon_F]A[\epsilon_\beta(\mathbf{k}+\mathbf{G}_{ij}),\epsilon_F], \quad (20)$$

where $g_s = 2$ and $g_v = 2$ account for the spin and valley degeneracy, respectively, and $\mathcal{A}$ is the cross-sectional area. A is the spectral function approximated by a Lorentzian function near the Fermi energy [32] with a broadening lifetime that is the same as that used in the NEGF calculations.

To better understand the effect of the rotation, we divide the conductance into three parts

$$G = G_{i=j} + G_{i\neq j}^{\alpha=\beta} + G_{i\neq j}^{\alpha\neq\beta}, \quad (21)$$

where the first part

$$G_{i=j} = \frac{e^2 g_s g_v}{\hbar} \sum_{\substack{\mathbf{k},\alpha\,=\,\beta \\ i\,=\,j\,=\,1,2,3}} \left|t_{i,j}^{\alpha,\beta}(\mathbf{k},\mathbf{k})\right|^2 A^2[\epsilon(\mathbf{k}),\epsilon_F] \quad (22)$$

represents the coherent transport process where the momentum is conserved between top and bottom graphene layers. The second and third terms correspond to umklapp processes in which the second term is an intraband process

$$G_{i\neq j}^{\alpha=\beta} = \frac{e^2 g_s g_v}{\hbar\mathcal{A}} \sum_{\substack{\mathbf{k},\alpha\,=\,\beta \\ i\,\neq\,j\,=\,1,2,3}} \left|t_{i,j}^{\alpha,\beta}(\mathbf{k},\mathbf{k}+\mathbf{G}_{ij})\right|^2 \times A[\epsilon_\alpha(\mathbf{k}),\epsilon_F]A[\epsilon_\alpha(\mathbf{k}) + \alpha\hbar\upsilon\sqrt{3}k_D\theta,\epsilon_F], \quad (23)$$

and the third term is an interband process,

$$G_{i\neq j}^{\alpha\neq\beta} = \frac{e^2 g_s g_v}{\hbar} \sum_{\substack{\mathbf{k},\alpha\,\neq\,\beta \\ i\,\neq\,j\,=\,1,2,3}} \left|t_{i,j}^{\alpha,\beta}(\mathbf{k},\mathbf{k}+\mathbf{G}_{ij})\right|^2 A[\epsilon_\alpha(\mathbf{k}),\epsilon_F] \times A[\epsilon_\beta(\mathbf{k}) + \beta(\hbar\upsilon\sqrt{3}k_D\theta - 2\epsilon_F),\epsilon_F]. \quad (24)$$

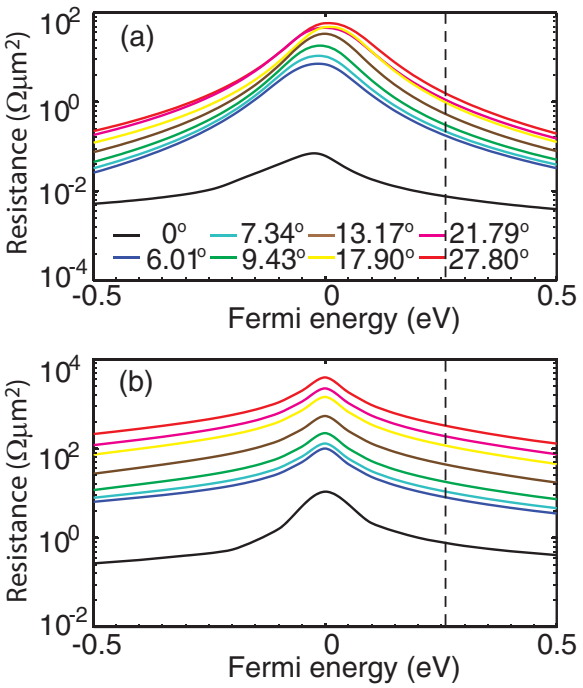

FIG. 2. Zero-temperature coherent resistance of twisted (a) Gr/1 layer h-BN/Gr heterostructure and (b) Gr/3 layer h-BN/Gr heterostructure as a function of Fermi energy for different commensurate rotation angles. The dashed line shows the Fermi energy of 0.26 eV used to calculate the resistance values in Fig. 3. The resistances are calculated from the tight-binding, NEGF approach.

III. RESULTS

Figure 2 shows the tight-binding, NEGF calculations of the zero-temperature, coherent resistance versus Fermi energy (E_F) for heterostructures with (a) a single h-BN layer and (b) three h-BN layers. The Fermi level E_F varies from -0.5 to 0.5 eV around the charge neutrality point for a range of rotation angles from 0° to 27.79° as indicated in the legend. The lowest black curve is the coherent resistance for the ABA unrotated heterostructure. For all of the angles shown, the resistance monotonically falls as the Fermi level moves away from the charge neutrality point where the density of states of the graphene layers is a minimum. In contrast to rotated bilayer graphene (r-BLG), for the two lowest angles 6.01° and 7.34°, there is no sudden change in resistance with Fermi energy around 0.3–0.4 eV [compare with Figs. 2(a) and 2(b) of Ref. [13]].

The vertical dashed lines in Fig. 2 correspond to a Fermi level of 0.26 eV. This is the Fermi level previously used for comparisons of the interlayer conductivity of misoriented bilayer graphene [11–13]. The numerical values of the resistance at $E_F = 0.26$ eV are given in Table II in Appendix B. As the h-BN layer becomes misaligned, the resistances increase by factors of 200 and 430 for the monolayer and trilayer h-BN structures, respectively. This trend in the variation of resistance with rotation angle is similar to the experimental observations in Ref. [14]. There, it was shown that the conductance can vary by a factor of 100 for different devices with the same h-BN thickness. For both the monolayer and trilayer h-BN structures, the increase in the resistance is a monotonic function of the

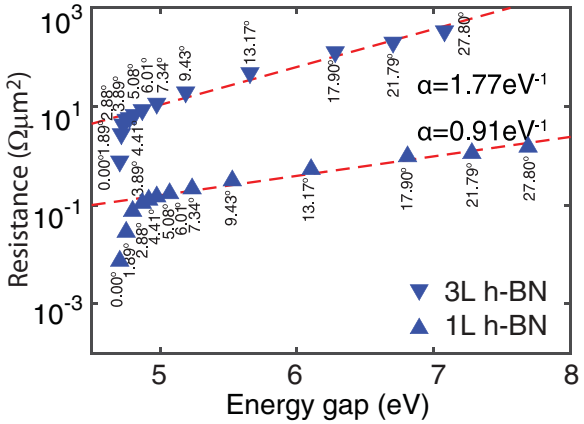

FIG. 3. Zero-temperature coherent resistance of graphene/1 layer h-BN/graphene (upward-pointing triangles) and graphene/3 layer h-BN/graphene (downward-pointing triangles) as a function of the effective energy gap of the monolayer h-BN and three-layer h-BN at the K point of the graphene. The angles are given next to each data point. The red lines show exponential fits to the data, $R = R_0 e^{\alpha E_G}$. The values of α are shown next to the fitted line. $E_F = 0.26$ eV.

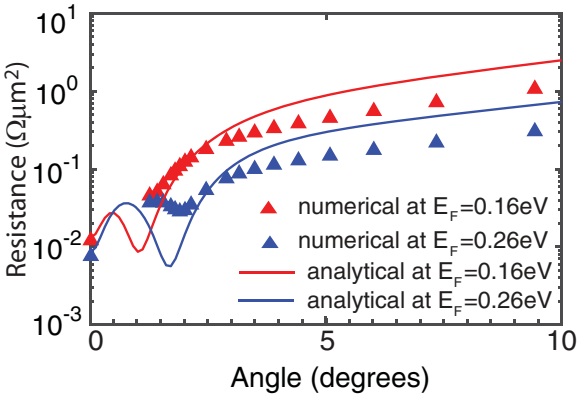

FIG. 4. Zero-temperature coherent resistance of Gr/1 layer h-BN/Gr as a function of rotation angle for Fermi energies equal to 0.26 eV (blue) and 0.16 eV (red). The solid lines show the results calculated from the continuum model, and the triangles show the results from the tight-binding, NEGF calculation. The smallest commensurate rotation angle calculated numerically is 1.25°.

h-BN rotation angle as the rotation angle increases from 6° to 27.79°. This trend is also in contrast to that of r-BLG. In the r-BLG system, at low energies near the charge neutrality point, the coherent interlayer resistance is a monotonic function of the supercell lattice constant as opposed to the rotation angle [compare to Fig. 1(d) of Ref. [12]].

To investigate process (b) in which rotation of the h-BN alters the tunnel barrier, we calculate the energy gap of ML and trilayer h-BN at the h-BN k point corresponding to graphene's K point as a function of rotation angle as illustrated in Fig. 1(b). The resulting effective band gap for ML h-BN is plotted versus rotation angle in Fig. 1(c). Since the direct band gap (4.7 eV) of h-BN occurs at its K point, the minimum h-BN band gap "seen" by an electron at the K point in the graphene layer occurs for h-BN rotation angles of 0° and 60° when graphene's K point is aligned with h-BN K or K' points. The effective h-BN band gap seen by an electron at the K point in the graphene layer monotonically increases as the h-BN is rotated from $\theta = 0°$, and it reaches a maximum at $\theta = 30°$. In the Brillouin zone of the h-BN, this corresponds to the band gap near the M point. This monotonic increase in the tunnel barrier with angle follows the same monotonic trend as the increase in resistance with angle.

To analyze the relation between the effective energy gap and resistance, we show in Fig. 3 a semilog plot of the resistance as a function of the effective h-BN band gap (for different rotation angles) at $E_F = 0.26$ eV. For angles greater than 4°, the tunnel current scales exponentially with the effective band gap as one would expect for tunneling through a potential barrier. Therefore, for $\theta > 4°$, we find that the dominant process affecting the tunnel current is the change in the effective h-BN band gap "seen" by the electrons at the K point in graphene.

However, for small angles $\theta < 4°$, there is clearly a very different trend and a different dependence of the resistance on the h-BN rotation angle. The different dependencies arise from different parallel conductance channels that dominate at different angle regimes. To analyze the low-angle region of the curve, we turn to the effective continuum model.

A more detailed picture of the low-angle regime is given in Fig. 4 which shows the resistance versus h-BN rotation angle calculated with both the continuum model and the NEGF tight-binding model for two values of E_F. The solid lines are from the continuum model, and the triangles are from the NEGF, tight-binding model. More low angles are included in the NEGF calculations, and the smallest rotated angle calculated from the NEGF, tight-binding model is 1.25°. Both models show a nonmonotonic dependence of resistance on angle at very low angles $\theta < 2.5°$. While the magnitudes differ between the two models, the overall trends match well.

The continuum model tells us that there are three parallel conductance channels corresponding to the direct and two umklapp processes in Eqs. (21)–(24). The individual channels dominate in different angle regimes. The angle at which each channel dominates is primarily determined by the overlap of the spectral functions in Eqs. (22)–(24). For the direct term, $G_{i=j}$ of Eq. (22), the spectral functions always overlap since the top and bottom graphene layers are aligned. For the two umklapp terms, the overlaps of the spectral functions are functions of the angles, and the overlaps become negligible for $\hbar\upsilon\sqrt{3}k_D\theta >> \hbar/\tau, \epsilon_F$. Therefore, for larger angles, $\theta > 4°$, the direct channel dominates, and the dependence on the angle is through the matrix element which, through $\mathbf{H}_{\mathrm{BN}}(\mathbf{k})$ and the effective interaction, includes the effect of the increase in the apparent h-BN band gap with angle as described above and shown in Fig. 1(c).

The maximum overlap of the spectral functions in the "interband" term of Eq. (24) occurs when $\hbar\upsilon\sqrt{3}k_D\theta = 2\epsilon_F$. This term is maximum at rotation angle $\theta_m = 2\epsilon_F/\hbar\upsilon\sqrt{3}k_D$, and it decreases for angles greater than or less than θ_m. This interband term is responsible for the dip in resistance for θ between 1° and 2° in Fig. 4. It also explains the shift in angle with Fermi level. As the Fermi level is increased, the local minimum moves to larger rotation angles since the angle of maximum overlap θ_m is linearly proportional to ϵ_F.

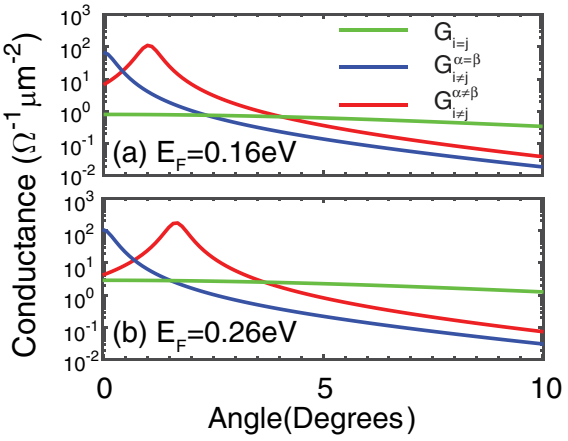

FIG. 5. Conductance components as a function of rotation angle for (a) $E_F = 0.16$ eV, (b) $E_F = 0.26$ eV.

The maximum overlap of the spectral functions in the "intraband" term of Eq. (23) occurs at $\theta = 0$. As θ increases, this channel monotonically decreases with the decrease governed by the decreasing overlap of the spectral functions. Since this channel has a maximum as θ goes to zero, it governs the initial increase in resistance for the smallest angles. The three individual contributions to the continuum model (direct, interband, and intraband, are shown in Fig. 5 for the two different Fermi levels, 0.26 and 0.16 eV.

While analyzing the resistance as a function of rotation angle is useful for clarifying the physics, verifying the trends shown in Fig. 4 would be very difficult experimentally. Experimentally, it is far easier to fix the angle and sweep the Fermi level of the top and bottom graphene layers. The resulting resistances calculated both from the NEGF, tight-binding and the continuum models for a 1-ML h-BN rotation angle of 3.89° are shown in Fig. 6(a).

Both models show nonmonotonic behavior of the resistance as the Fermi level is swept between 0.5 and 0.6 eV. To observe this feature at lower Fermi levels, a smaller angle is required, and to observe the feature experimentally a larger resistance

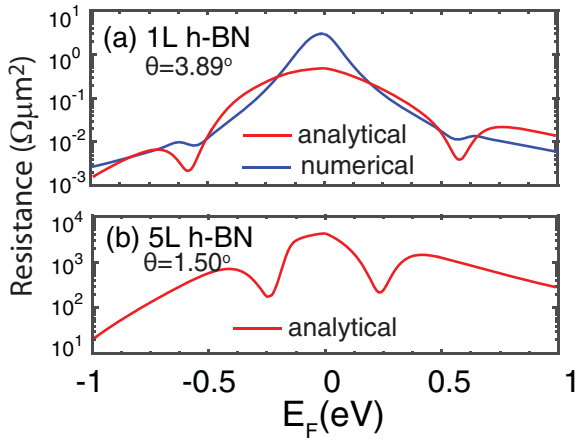

FIG. 6. Resistance versus Fermi level of the Gr/1 layer h-BN/Gr structure (a) calculated by both the continuum model and the NEFG method with $\theta = 3.89°$, and (b) calculated by the continuum model only with $\theta = 1.50°$.

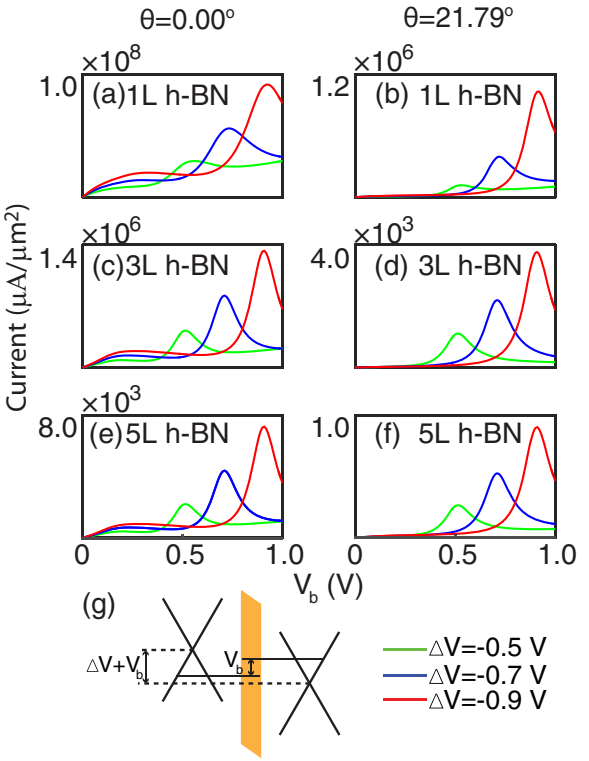

FIG. 7. Current as a function of bias voltage for different potential differences ΔV between the two graphene layers. (a) Graphene/1 layer h-BN/graphene with no rotation; (b) graphene/1 layer h-BN/graphene with a 21.79° rotation angle; (c) graphene/3 layer h-BN/graphene with no rotation; (d) graphene/3 layer h-BN/graphene with a 21.79° rotation angle; (e) graphene/5 layer h-BN/graphene with no rotation; (f) graphene/5 layer h-BN/graphene with a 21.79° rotation angle.

is required. The larger resistance is achieved by increasing the number of h-BN layers from 1 to 5. The resistance versus Fermi level calculated from the continuum model for a 5-ML h-BN layer rotated by 1.50° is shown in Fig. 6(b). The nonmonotonic feature moves to lower energies and now occurs as the Fermi level is swept between 0.2 and 0.3 eV. The overall magnitude of the resistance is between 100 and 1000 $\Omega\mu m^2$ which should be large enough to be observable, and it can be increased by increasing the number of h-BN layers.

So far, we have focused on the zero-bias resistivity to elucidate the physics. However, interest in this system is driven by potential applications, and one application of current investigation is a high-frequency oscillator that exploits the negative differential resistance observed under high bias. To understand how the misorientation of the h-BN layer affects the current-voltage (I-V) characteristic of this structure, we show in Fig. 7 the NEGF, tight-binding calculations using Eq. (8) of the I-V characteristics for the unrotated structure and the structure with the h-BN layer rotated by 21.78° for h-BN layer thicknesses of 1, 3, and 5 ML. The three I-V characteristics in each plot are for three different built-in potentials ΔV between the two graphene layers. The panels on the left are for the unrotated structure while the panels on the right are for the 21.79° structure. In Figs. 7(a) and 7(b), it is shown that the rotation of monolayer h-BN decreases the current by

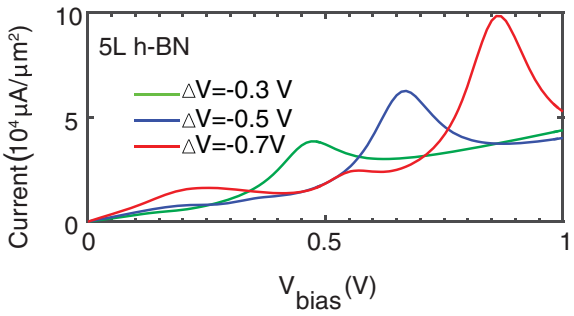

FIG. 8. Current as a function of bias voltage for different potential differences ΔV between the two graphene layers for the 5 layer h-BN structure with a h-BN rotation angle of $\theta = 0.5^\circ$.

nearly two orders of magnitude. This relative decrease in the tunneling current becomes progressively greater as the number of h-BN layers is increased, as shown in the other subplots. For the case of five h-BN layers, the tunneling current is nearly four orders of magnitude smaller. As expected, this decrease in the tunneling current and its scaling is consistent with the resistance increasing with the rotation angles as shown in Fig. 2. While the current decreases with rotation angle, the peak-to-valley current ratio is unaffected.

For small rotation angles, it is interesting to consider whether new qualitative features appear in the nonlinear I-V characteristic. To answer that question, we applied the effective continuum model to calculate I-V curves of a structure with $\theta = 0.5^\circ$. The results in Fig. 8, for three different values of built-in voltage ΔV, are qualitatively different from the I-V curves for large-angle rotation since several regions of NDR appear depending on the initial built-in potential. The first and third peaks arise from the interband component which is maximum at $V_{\text{bias}} = \pm\hbar v\sqrt{3}k_D\theta - \Delta V$. The middle peak that occurs at $V_{\text{bias}} = -\Delta V$ is caused by the direct tunneling term.

The model used for these calculations does not include lattice mismatch between the graphene and the h-BN since that prohibits the creation of a commensurate unit cell required for the numerical tight-binding calculations. If we consider the lattice mismatch in the effective continuum model, the size of commensurate Brillouin zone will change from $k_D\theta$ to $k_D\sqrt{\theta^2+\delta^2}$, where δ is the lattice mismatch between the graphene and the h-BN. The mismatch $k_D\sqrt{\theta^2+\delta^2}$ will still decrease monotonically with a decrease in the rotation angle. Therefore, the relation between conductance and rotation angle is qualitatively the same as the angle is decreased. The only difference is that in the small-angle region, $k_D\sqrt{\theta^2+\delta^2}$ decreases more slowly than $k_D\theta$, and it has a minimum value $k_D\delta$ when the angle is zero.

IV. CONCLUSIONS

Electron transport through a Gr/h-BN/Gr structure is examined within a tight-binding model with commensurate rotation angles and within an effective continuum model. The two graphene layers are aligned, and the h-BN layer is rotated by an angle θ with respect to the graphene layers. For angles greater than 4°, the resistance is dominated by the change in the effective h-BN band gap seen by an electron at the K point of the graphene. In this large-angle regime, the effect of rotating the h-BN is to increase the barrier height of the h-BN tunnel barrier at the K point of the graphene. For $\theta \gtrsim 4^\circ$, the resistance monotonically increases with the rotation angle, and it reaches a maximum at $\theta = 30^\circ$. As θ is increased from 0° to 30°, the coherent interlayer resistance increases by factors of 200 and 430 for monolayer and trilayer h-BN layers, respectively. For devices that exhibit NDR under high bias, rotation of the h-BN primarily serves to reduce the overall magnitude of the current. It does not degrade the peak-to-valley current ratios. In this large-angle regime, since the dominant physics is that of single-barrier direct tunneling, phonon scattering should have negligible effect on the low-bias, angle-dependent trends and magnitudes of the interlayer resistances. Since NDR results from momentum conservation, phonon scattering will reduce the peak-to-valley ratios, but this effect also exists in the unrotated structure. While we do not expect a significant dependence of the phonon scattering on the rotation angle of the h-BN in the large-angle regime, this is an open question for further study.

The small-angle regime ($\theta \lesssim 4^\circ$) reveals qualitatively new features both in the low-bias interlayer resistances and in the high-bias I-V characteristics. The new features arise due to the opening of new conductance channels corresponding to umklapp processes. With the two graphene layers aligned, umklapp processes give rise to two new conduction channels corresponding to an intraband term and an interband term. The angular and energy dependence of these terms is primarily determined by the overlap of the top and bottom graphene spectral functions that are shifted in momentum space with respect to each other by an umklapp lattice vector. For a fixed rotation angle θ of the h-BN layer, both the intraband and interband terms peak at a Fermi level $\varepsilon_F^m \equiv \hbar v k_D\theta\sqrt{3}/2$. At this Fermi level, the two spectral functions in the interband term perfectly overlap, so that the interband term dominates. This strong peak in the interband term results in a distinct, nonmonotonic feature in a plot of the interlayer resistance versus Fermi energy that occurs as the Fermi level is swept through $\pm\varepsilon_F^m$. The qualitative trends of this nonmonotonic feature are reproduced in the tight-binding calculations for structures with small commensurate rotation angles, although the overall magnitude of the feature is less. The interband term also gives rise to two extra peaks in the nonlinear I-V characteristic on either side of the peak resulting from the direct tunneling term. Amorim *et al.* [35] found that phonon scattering and incoherent scattering in this low-angle regime reduces the magnitude of the features resulting from umklapp processes, but it does not remove them, so that the new features in the low-angle regime should be experimentally observable.

ACKNOWLEDGMENTS

This work is supported in part by FAME, one of six centers of STARnet, a Semiconductor Research Corporation program sponsored by MARCO and DARPA and the NSF Grant No. EFRI-1433395. This work used the Extreme Science and Engineering Discovery Environment (XSEDE), which is supported by National Science Foundation Grant No. ACI-1053575.

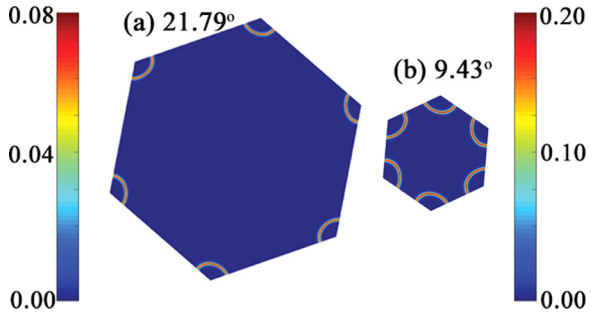

FIG. 9. Transmission coefficient $T(E,\mathbf{k})$ in the first Brillouin at energy of 0.5 eV for graphene/1 layer h-BN/graphene heterostructure with rotation angle (a) 21.79°, (b) 9.43°.

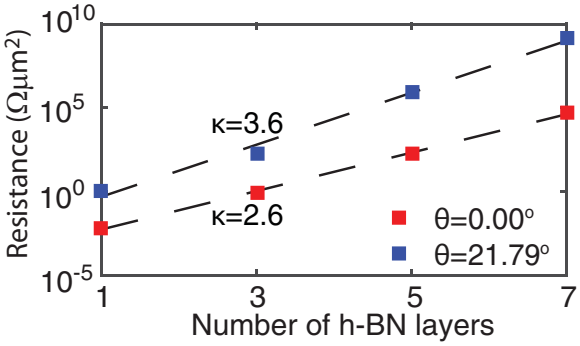

FIG. 10. Resistance versus number of h-BN layers for rotation angles of 0.00° and 21.79° at a Fermi energy of $E_F = 0.26$ eV. The dashed lines show the exponential fits $R = R_0 e^{\kappa \cdot n}$ where n is the number of h-BN layers. The decay constants κ are shown next to the fits for the two structures.

APPENDIX A: TIGHT-BINDING MODEL AND METHOD DETAILS

The transmission coefficient over $\mathbf{k}$ in the first Brillouin zone $T(E) = \int_{1\text{st BZ}} \frac{d^2\mathbf{k}}{4\pi^2} T(E,\mathbf{k})$ was numerically integrated on a square grid with $\Delta k_x = \Delta k_y = 0.005$ Å^{-1}. Figure 9 shows the momentum-resolved transmission $T(E,\mathbf{k})$ in the first Brillouin zone corresponding to the two commensurate rotation angles of 21.79° and 9.43° at $E = 0.5$ eV. The transmission is centered at the K and K' and peaks on the isoenergy surface.

To extract a tunneling decay constant of the h-BN predicted by the interlayer tight-binding parameters, we calculate the resistance of 1, 3, 5, and 7 layers of h-BN for two angles of $\theta = 0°$ and $\theta = 21.79°$ at $E_F = 0.26$ eV. Figure 10 shows the exponential increase in resistance with increasing number of h-BN layers for both structures. Fitting the results to an exponential function $R = R_0 e^{\kappa \cdot n}$, where n is the number of h-BN layers, gives values for κ of 2.6 and 3.6 for the unrotated and rotated structures, respectively. These values are similar to an experimentally extracted value of $\kappa = 4.0$ [41].

APPENDIX B: RESULTS OF RESISTANCE AS A FUNCTION OF ROTATION ANGLE

The numerical values of the resistance at $E_F = 0.26$ eV are given in Table II.

TABLE II. Effective h-BN energy gap and the coherent resistances at $E_F = 0.26$ eV for different commensurate rotation angles and two different h-BN thicknesses of 1 and 3 ML. The resistances are calculated from the tight-binding, NEGF approach.

	Gr/1 layer h-BN/Gr		Gr/3 layer h-BN/Gr	
θ (degrees)	Energy gap (eV)	Resistance ($\Omega\mu$m^2)	Energy gap (eV)	Resistance ($\Omega\mu$m^2)
0.00	4.709	0.007601	4.709	0.7972
1.25	4.726	0.03710		
1.41	4.730	0.03758		
1.54	4.734	0.03711		
1.61	4.737	0.03521		
1.70	4.740	0.03308		
1.79	4.743	0.03028		
1.89	4.748	0.02844	4.713	2.752
2.00	4.752	0.02954		
2.13	4.758	0.03481		
2.45	4.774	0.05355		
2.88	4.798	0.07565	4.726	4.474
3.15	4.815	0.08741		
3.48	4.838	0.09981		
3.89	4.869	0.1132	4.753	5.510
4.41	4.913	0.1288	4.774	6.094
5.08	4.976	0.1481	4.807	6.977
6.01	5.075	0.1753	4.865	8.495
7.34	5.237	0.2182	4.971	11.43
9.43	5.529	0.3048	5.184	18.87
13.17	6.106	0.5371	5.653	46.48
17.90	6.813	0.9770	6.274	123.6
21.79	7.280	1.120	6.701	199.7
27.80	7.686	1.563	7.073	344.3

[1] K. S. Novoselov, V. Fal, L. Colombo, P. Gellert, M. Schwab, and K. Kim, Nature (London) **490**, 192 (2012).

[2] A. H. Castro Neto, F. Guinea, N. M. R. Peres, K. S. Novoselov, and A. K. Geim, Rev. Mod. Phys. **81**, 109 (2009).

[3] C. R. Dean, A. F. Young, I. Meric, C. Lee, L. Wang, S. Sorgenfrei, K. Watanabe, T. Taniguchi, P. Kim, and K. Shepard, Nat. Nanotechnol. **5**, 722 (2010).

[4] J. Xue, J. Sanchez-Yamagishi, D. Bulmash, P. Jacquod, A. Deshpande, K. Watanabe, T. Taniguchi, P. Jarillo-Herrero, and B. J. LeRoy, Nat. Mater. **10**, 282 (2011).

[5] C. Hwang, D. A. Siegel, S.-K. Mo, W. Regan, A. Ismach, Y. Zhang, A. Zettl, and A. Lanzara, Sci. Rep. **2**, 590 (2012).

[6] B. Hunt, J. D. Sanchez-Yamagishi, A. F. Young, M. Yankowitz, B. J. LeRoy, K. Watanabe, T. Taniguchi, P. Moon, M. Koshino, P. Jarillo-Herrero, and R. C. Ashoori, Science **340**, 1427 (2013).

[7] J. C. W. Song, A. V. Shytov, and L. S. Levitov, Phys. Rev. Lett. **111**, 266801 (2013).

[8] X. Zhao, L. Li, and M. Zhao, J. Phys.: Condens. Matter **26**, 095002 (2014).

[9] C. R. Woods, L. Britnell, A. Eckmann, R. S. Ma, J. C. Lu, H. M. Guo, X. Lin, G. L. Yu, Y. Cao, R. V. Gorbachev, A. V. Kretinin, J. Park, L. A. Ponomarenko, M. I. Katsnelson, Y. N. Gornostyrev, K. Watanabe, T. Taniguchi, C. Casiraghi, H.-J. Gao, A. K. Geim, and K. S. Novoselov, Nat. Phys. **10**, 451 (2014).

[10] J. Jung, A. DaSilva, A. H. MacDonald, and S. Adam, Nat. Commun. **6**, 6308 (2015).

[11] R. Bistritzer and A. H. MacDonald, Phys. Rev. B **81**, 245412 (2010).

[12] V. Perebeinos, J. Tersoff, and P. Avouris, Phys. Rev. Lett. **109**, 236604 (2012).

[13] K. M. M. Habib, S. S. Sylvia, S. Ge, M. Neupane, and R. K. Lake, Appl. Phys. Lett. **103**, 243114 (2013).

[14] L. Britnell, R. V. Gorbachev, R. Jalil, B. D. Belle, F. Schedin, A. Mishchenko, T. Georgiou, M. I. Katsnelson, L. Eaves, S. V. Morozov, N. M. R. Peres, J. Leist, A. K. Geim, K. S. Novoselov, and L. A. Ponomarenko, Science **335**, 947 (2012).

[15] T. Georgiou, R. Jalil, B. D. Belle, L. Britnell, R. V. Gorbachev, S. V. Morozov, Y.-J. Kim, A. Gholinia, S. J. Haigh, O. Makarovsky, L. Eaves, L. A. Ponomarenko, A. K. Geim, K. S. Novoselov, and A. Mishcheno, Nat. Nanotechnol. **8**, 100 (2012).

[16] R. M. Feenstra, D. Jena, and G. Gu, J. Appl. Phys. **111**, 043711 (2012).

[17] L. Britnell, R. V. Gorbachev, A. K. Geim, L. A. Ponomarenko, A. Mishchenko, M. T. Greenaway, T. M. Fromhold, K. S. Novoselov, and L. Eaves, Nat. Commun. **4**, 1794 (2013).

[18] L. A. Ponomarenko, B. D. Belle, R. Jalil, L. Britnell, R. V. Gorbachev, A. K. Geim, K. S. Novoselov, A. H. Castro Neto, L. Eaves, and M. I. Katsnelson, J. Appl. Phys. **113**, 136502 (2013).

[19] P. Zhao, R. M. Feenstra, G. Gu, and D. Jena, IEEE Trans. Electron Devices **60**, 951 (2013).

[20] A. Mishchenko, J. S. Tu, Y. Cao, R. V. Gorbachev, J. R. Wallbank, M. T. Greenaway, V. E. Morozov, S. V. Morozov, M. J. Zhu, S. L. Wong, F. Withers, C. R. Woods, Y. Kim, K. Watanabe, T. Taniguchi, E. E. Vdovin, O. Makarovsky, T. M. Fromhold, V. I. Fal'ko, A. K. Geim, L. Eaves, and K. S. Novoselov, Nat. Nanotechnol. **9**, 808 (2014).

[21] M. T. Greenaway, E. E. Vdovin, A. Mishchenko, O. Makarovsky, A. Patane, J. R. Wallbank, Y. Cao, A. V. Kretinin, M. J. Zhu, S. V. Morozov, V. I. Falrsquorko, K. S. Novoselov, A. K. Geim, T. M. Fromhold, and L. Eaves, Nat. Phys. **11**, 1057 (2015).

[22] F. T. Vasko, Phys. Rev. B **87**, 075424 (2013).

[23] T. Roy, L. Liu, S. de la Barrera, B. Chakrabarti, Z. R. Hesabi, C. A. Joiner, R. M. Feenstra, G. Gu, and E. M. Vogel, Appl. Phys. Lett. **104**, 123506 (2014).

[24] B. Fallahazad, K. Lee, S. Kang, J. Xue, S. Larentis, C. Corbet, K. Kim, H. C. P. Movva, T. Taniguchi, K. Watanabe, L. F. Register, S. K. Banerjee, and E. Tutuc, Nano Lett. **15**, 428 (2015).

[25] Y. Zhao, Z. Wan, X. Xu, S. R. Patil, U. Hetmaniuk, and M. P. Anantram, Sci. Rep. **5**, 10712 (2015).

[26] J. Gaskell, L. Eaves, K. S. Novoselov, A. Mishchenko, A. K. Geim, T. M. Fromhold, and M. T. Greenaway, Appl. Phys. Lett. **107**, 103105 (2015).

[27] T. L. M. Lane, J. R. Wallbank, and V. I. Fal'ko, Appl. Phys. Lett. **107**, 203506 (2015).

[28] S. C. de la Barrera and R. M. Feenstra, Appl. Phys. Lett. **106**, 093115 (2015).

[29] S. C. de la Barrera, Q. Gao, and R. M. Feenstra, J. Vac. Sci. Technol. B **32**, 04E101 (2014).

[30] L. Brey, Phys. Rev. Appl. **2**, 014003 (2014).

[31] E. E. Vdovin, A. Mishchenko, M. T. Greenaway, M. J. Zhu, D. Ghazaryan, A. Misra, Y. Cao, S. V. Morozov, O. Makarovsky, T. M. Fromhold, A. Patanè, G. J. Slotman, M. I. Katsnelson, A. K. Geim, K. S. Novoselov, and L. Eaves, Phys. Rev. Lett. **116**, 186603 (2016).

[32] K. A. Guerrero-Becerra, A. Tomadin, and M. Polini, Phys. Rev. B **93**, 125417 (2016).

[33] S. B. Kumar, G. Seol, and J. Guo, Appl. Phys. Lett. **101**, 033503 (2012).

[34] S. Hwan Lee, M. Sup Choi, J. Lee, C. Ho Ra, X. Liu, E. Hwang, J. Hee Choi, J. Zhong, W. Chen, and W. Jong Yoo, Appl. Phys. Lett. **104**, 053103 (2014).

[35] B. Amorim, R. M. Ribeiro, and N. M. R. Peres, Phys. Rev. B **93**, 235403 (2016).

[36] S. Shallcross, S. Sharma, E. Kandelaki, and O. A. Pankratov, Phys. Rev. B **81**, 165105 (2010).

[37] R. M. Ribeiro and N. M. R. Peres, Phys. Rev. B **83**, 235312 (2011).

[38] G. Klimeck, R. Lake, R. C. Bowen, W. R. Frensley, and T. Moise, Appl. Phys. Lett. **67**, 2539 (1995).

[39] R. Bistritzer and M. A. H, Proc. Natl. Acad. Sci. USA **108**, 12233 (2011).

[40] M. Kindermann, B. Uchoa, and D. L. Miller, Phys. Rev. B **86**, 115415 (2012).

[41] L. Britnell, R. V. Gorbachev, R. Jalil, B. D. Belle, F. Schedin, M. I. Katsnelson, L. Eaves, S. V. Morozov, A. S. Mayorov, N. M. R. Peres, A. H. C. Neto, J. Leist, A. K. Geim, L. A. Ponomarenko, and K. S. Novoselov, Nano Lett. **12**, 1707 (2012).